

High-Temperature Thermal Transport in Porous Silica Materials: Direct Observation of a Switch from Conduction to Radiation

Anna M. Neuhöfer, Kai Herrmann, Flora Lebeda, Tobias Lauster, Christoph Kathmann, Svend-Age Biehs,* and Markus Retsch*

Efficient thermal insulation at high temperatures poses stringent requirements on suitable materials. Low density, porous inorganic structures with pore sizes in the sub-micrometer range are of particular interest for such materials to control heat conduction. Simultaneously, thermal radiation has to be suppressed, which depends on the optical properties of the constituents. Here, the authors demonstrate a direct observation of the transition from a conduction dominated to a radiation dominated thermal transport mechanism for the case of particulate silica materials at temperatures reaching up to 925 °C. A detailed analysis of the radiative transport through bulk silica as well as solid and hollow silica particles is provided. Optical transparency at high temperatures is the driving force, whereas surface wave modes barely contribute, particularly in case of the insulating particle packings. The existing analytical framework of laser flash analysis is extended to qualitatively describe the radiative and conductive heat transport by two independent diffusive transport models. The analysis provides a better understanding of the challenges to fabricate and analyze efficient thermal insulation materials at high operating temperatures, where multiple heat transport mechanisms need to be controlled.

gas industry, and aerospace components. Aerogels—typically made from carbon or silica—are compelling materials for thermal insulation. Especially, silica is suitable for thermal applications owing to its low thermal conductivity, high melting temperature, and chemical inertness. Furthermore, silica is naturally abundant and can be recycled after usage.

Colloidal structures based on hollow silica spheres can be regarded as high-density aerogels with a hierarchical pore structure. Aerogels have densities between 1 and 1000 kg m⁻³,^[1] while the density of hollow silica particle assemblies is in the range of 180 to 883 kg m⁻³.^[2] Colloidal assemblies have the advantage of easier fabrication due to the absence of a supercritical drying procedure. Furthermore, their well-defined pore sizes simplify the determination of structure–property relationships.

Most of the thermal insulation applications of aerogel materials have been considered at ambient temperatures. However, heat insulation at high operating temperatures is of great relevance for power plants, manufacturers, and aerospace. The thermal properties of insulating samples at high temperatures have been typically determined by the hot wire or hot plate techniques.^[3] One drawback of these techniques is that relatively large samples with diameters up to 20 cm and several centimeter thicknesses are needed for the measurements. In case of the transient hot disc method, even two identical specimens are required. Therefore, high-temperature (HT) laser flash analysis (LFA) would be an interesting alternative, because just one sample with a diameter of 1 cm and a few mm thickness is needed. The LFA method has been well-established for room temperature (RT) measurements on a wide range of samples, including composites, monoliths, polymers, to name a few. Ruckdeschel et al. performed LFA on colloidal crystals from hollow silica nanoparticles and examined the thermal transport mechanisms.^[2,4] While Ruckdeschel et al. examined the size range of 250–500 nm, Mofid et al. examined the thermal properties of the sub 100 nm region.^[5] There are few cases where LFA was used for aerogel samples up to 1500°C. They have been performed by Wiener et al.^[6] and Feng et al.^[7] However, the groups

1. Introduction

Thermal insulation plays an enormous role in various applications in everyday life, like buildings, automobiles, the oil and

A. M. Neuhöfer, K. Herrmann, F. Lebeda, T. Lauster, M. Retsch
Department of Chemistry
Physical Chemistry I
University of Bayreuth
95440 Bayreuth, Germany
E-mail: markus.retsch@uni-bayreuth.de

C. Kathmann, S.-A. Biehs
Institut für Physik
Carl von Ossietzky Universität
26111 Oldenburg, Germany
E-mail: s.age.biehs@uni-oldenburg.de

 The ORCID identification number(s) for the author(s) of this article can be found under <https://doi.org/10.1002/adfm.202108370>.

© 2021 The Authors. Advanced Functional Materials published by Wiley-VCH GmbH. This is an open access article under the terms of the Creative Commons Attribution License, which permits use, distribution and reproduction in any medium, provided the original work is properly cited.

DOI: 10.1002/adfm.202108370

used carbon aerogels, which render them opaque across a wide spectral range.

The overall thermal conductivity of porous materials, like aerogels and colloidal structures, can be described by three contributions: solid and gaseous conduction, and radiation. Solid conduction takes place in the amorphous silica matrix material. The microstructure of the materials dictates the thermal conductivity in the solid conduction case. Amorphous structures, inclusions of defects, or micropores reduce the thermal conductivity through the skeleton of the porous material.^[8]

Gaseous conduction takes place in the pores in the aerogel or between and in the (hollow) nanoparticles. It is strongly influenced by the Knudsen effect when the mean free path of the gas equals or exceeds the pore size of the surrounding system.^[9] For nitrogen gas, the mean free path is between 88 nm at 25 °C and 354 nm at 925 °C,^[10] precisely in the region of colloidal crystals under investigation here. Therefore, the Knudsen effect plays a significant role in gaseous conduction and is strongly reduced due to the strong confinement in pores smaller than 100 nm.

Radiation describes the effect of a surface emitting electromagnetic waves due to its temperature. This energy is absorbed by another surface and reemitted, and so forth.^[11] Every matter with temperatures above 0 K emits thermal radiation. An idealized object that absorbs all incident radiation and emits with an emissivity of unity is called a black body radiator. The emissive power of other surfaces is compared to this maximum performance and is a fraction of 1. For highly insulating applications, the contribution of thermal radiation shall be suppressed as much as possible. This is achieved for polymer foams and aerogels by the addition of opacifiers,^[12] like carbon,^[3b,d,13] or doping with materials such as Y₂O₃.^[14] The group of Prof. Fricke has developed a thorough understanding of heat transport in aerogels.^[3b,d,e] They found that for high-density aerogels, the solid conduction is the main transport path. Gaseous conduction and radiation become more critical with lower density. Heinemann et al. were able to show that there is a complex interaction of radiation and conduction inside the sample, while conduction predominates at the boundaries.^[3b,d] In the last 10 years, the theoretical description of radiative heat transfer in many-body systems, including the contribution of near-field effects, has made great progress.^[15] In particular, heat radiation in nanoparticle assemblies has been studied in a large number of works using the dipole approximation.^[16] Within this approximation, the radiative heat conductivity can be calculated in systems composed of several thousand or ten thousand nanoparticles.^[17] However, this method is strictly speaking, not applicable in dense colloids because higher multipole moments need to be included if the center-to-center distance between the nanoparticles is smaller than ~three to four times the particle radius^[18] which corresponds in a cubic lattice to a filling fraction of only 7% to 12%. Including these higher multipoles makes the theoretical evaluation of the heat conductivity in many-body systems difficult. Since our samples are relatively large and dense, we chose for the optical modeling, an effective multilayer approach similar to Sakatani et al.^[19] to calculate the radiative heat conductivity in powdered materials, but with the extension that we included near-field effects, that is, the contribution of evanescent waves.

Our investigation uses the time resolution of high-temperature LFA measurements to unravel the gradual transition

Table 1. Density, δ , thermal diffusivity, α , and thermal conductivity, κ , at 25 °C of the colloidal glasses from particles with diameter, d_{tot} , and shell thickness, d_s .

Sample	d_{tot} [nm]	d_s [nm]	δ [g cm ⁻³]	α [mm ² s ⁻¹]	κ [W mK ⁻¹]
SiO ₂ hollow small	278	29	0.594	0.251	0.111
SiO ₂ hollow big	882	31	0.219	0.226	0.037
SiO ₂ solid small	353		1.362	0.164	0.166
SiO ₂ solid big	889		1.347	0.113	0.113
SiO ₂ solid huge	8000		1.150	0.181	0.155

from solid conduction to radiative heat transport. We apply this unique advantage, which is not accessible by steady-state characterization methods, to colloidal glasses made from SiO₂ and TiO₂ solid and hollow particles. We work out the existence of these two transport processes in such porous materials and relate them to their optical properties.

2. Results and Discussion

We base our analysis on two types of porous silica materials, one comprising solid, the other comprising hollow spheres, owing to their high thermal insulation capability. We investigated for each type, two samples of comparable size ($d_{\text{tot}} \approx 300$ nm and $d_{\text{tot}} \approx 800$ nm) and complement this data set with one batch of large $\approx 8 \mu\text{m}$ sized solid silica beads. Owing to the filtration fabrication process, these particle assemblies can be considered colloidal glasses (Figure S3, Supporting Information). The key geometries and resulting density data are summarized in **Table 1**. We measured LFA on these SiO₂ hollow and solid particles in a temperature range from 25–925 °C (**Figure 1**).

We represent the raw data of the time-dependent temperature evolution on the top surface of the samples in a normalized fashion. Precisely, we normalized the intensity data by the maximum peak intensity because only the relative temperature change is relevant for our evaluation. We also normalized the timescale to better work out the two distinct transport mechanisms. Radiative and conductive heat transport occur at different characteristic time scales. By normalizing the time at 25 °C, $t_{c,25 \text{ °C}} = \frac{L^2}{\pi^2 \alpha}$, with the sample thickness, L , and the thermal diffusivity at 25 °C, α ; according to Cape and Lehmann, we remove any influence from the individual sample thickness.^[20] This way of time-normalization, consequently, renders the time-dependent measurements more comparable to one another. At room temperature, we observe only the conductive heat transport contribution. This is represented by the broad maximum, which slowly decays due to thermal losses to the sample holder and environment. This shape of the time-dependent temperature evolution is the classic case of an LFA experiment with solely conductive transport occurring through the sample. It can be well-fitted for all cases based on established models, which include the 1D heat diffusion equation in combination with certain loss mechanisms. For a detailed discussion and evaluation of the data fitting procedure in LFA experiments, we refer the reader to recent literature.^[21] The results for thermal diffusivity and thermal conductivity at 25 °C are

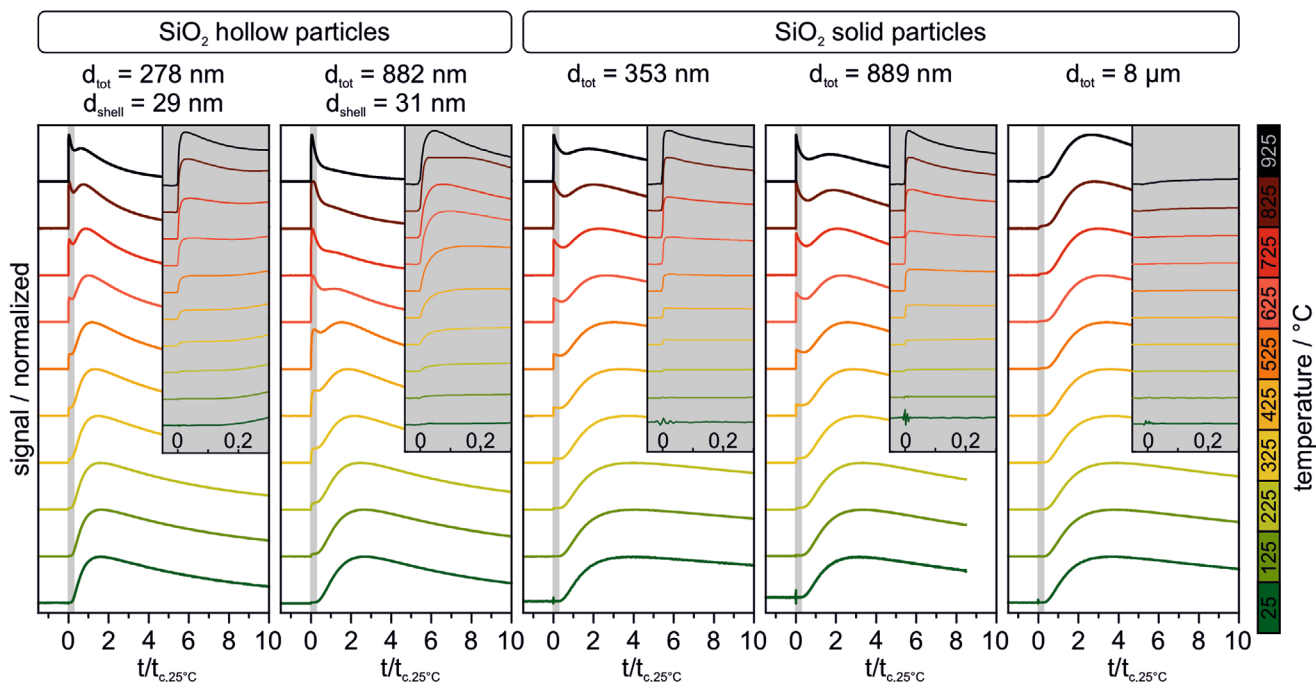


Figure 1. Temperature-dependent LFA measurement signal of SiO₂ hollow and solid particles. The grey insets show details of the radiation peak. The time data is normalized by the characteristic thermal response time t_c .

summarized in Table 1 and confirm the thermal insulation properties of such particle packings. In particular, the hollow sphere structures are strongly insulating. With increasing temperature, a second, much faster contribution starts to become more and more prominent in case of the sub- μm sized silica samples. Only the case of the 8 μm beads is still dominated by the slow process described by conduction through the particles. All other samples have two maxima – one sharp at $t/t_{c,25^\circ\text{C}} < 0.2$, and one broad maximum at $1 < t/t_{c,25^\circ\text{C}} < 4$, which we interpret as radiative and conductive transport as outlined below, respectively. The evolution of this fast heat transport is most pronounced for the 882 nm hollow particles, where at 925 °C, no conduction peak is visible anymore. The time-dependent temperature profiles that we consistently observed in our sub- μm granular samples are highly unusual in the case of LFA experiments and cannot be described by the established models. Quite frankly, such data are typically coined “bad” measurements and are not considered any further. To prove the correctness of our measurements, we performed additional tests to exclude any other sources that could lead to this unique time-dependent temperature evolution at the sample surface (Figure 2). We, therefore, measured reference materials with known thermal diffusivities and ruled out a potential influence from our tailor-made sample holder (Figure 2c). This sample holder was equipped with a graphite support, which was necessary to carry the samples, which were smaller than the contact face of the original holder. Furthermore, a spacer between the holder and the lid was required to reduce the mechanical load of the lid onto the sample, which would have led to a breakage of the sample.

Figure 2a shows the normalized measurement data, at 25 °C, 525 °C, and 925 °C for the original sample holder, with our

graphite support, and with the graphite spacer in combination with pyroceram as standard material. The measurement data show an identical time–temperature evolution regardless of the sample holder configuration. There is no evolution of a second peak discernible. Fitting of the thermal diffusivity for this standard material provided slightly varying thermal diffusivity data, which we attribute to changes of thermal losses into the holder. Overall, a good agreement between the measured and literature data was observed for this opaque standard material (Figure 2d). As a second class of reference material, we measured the properties of optically transparent bulk borosilicate and quartz glass (Figure 2b). The corresponding thermal diffusivities and literature values are shown in Figure 2e. Literature values for quartz glass have been calculated according to Sergeev et al.^[22] and match well with our measured data. Literature values for borosilicate glass were taken from Johnson et al.^[23] and are systematically higher compared to our data. We note, however, that borosilicate glass may differ depending on the supplier, which can explain the deviations to our data. The thermal diffusivity of borosilicate glass above 625 °C decreased, because the glass softened and changed its shape.

The major difference between the pyroceram and the glass measurements is the appearance of an increasing step at $t/t_{c,25^\circ\text{C}} < 0.1$ for temperatures exceeding 425 °C. In contrast to the data of the hollow and solid particle samples, this radiation step is well-known and can be confidently fitted by the “transparent model” developed from the manufacturer, taking into account radiative and conductive contributions. As outlined in Figure 2c, this steplike increase in temperature can be associated with radiative heat transport between the sample bottom and top surface. Thermalization of the Xenon light flash, as well as mid-infrared emission and absorption, respectively,

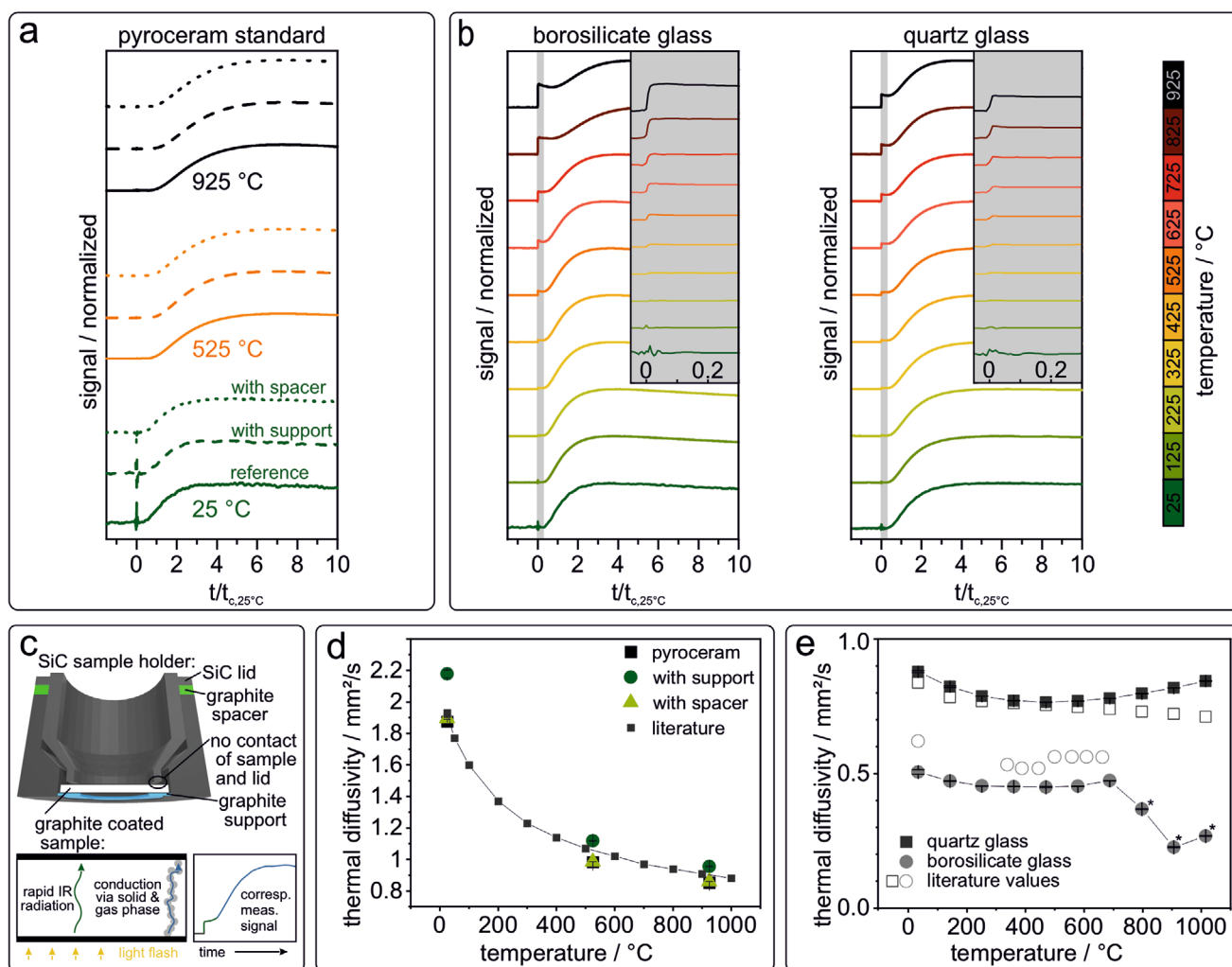


Figure 2. a) Temperature-dependent LFA signal of pyroceram standard, measured with modified LFA sample holder. d) The corresponding pyroceram thermal diffusivity, in comparison with literature values. b) Temperature-dependent LFA signal of bulk borosilicate glass and quartz glass measured with the modified sample holder. e) The corresponding thermal diffusivity, in comparison to literature values.^[22,23] c) Illustration of modified LFA sample holder, and sketch of heat transfer processes with the corresponding measurement signal in a LFA measurement.

happen much faster compared to the ms time resolution of the XFA experiment. Therefore, the sample's top surface temperature is offset by a small amount, which is accounted for by the fitting procedure. When comparing the insets of Figures 2b and 1, one recognizes a marked difference between the two early radiative events. A comparison of the radiation peak at $t/t_{c,25\text{ °C}} < 0.15$ is shown in Figure S5, Supporting Information. The granular samples demonstrate a marked loss in surface temperature after the initial increase, whereas the bulk material reaches a plateau. Even more important is the apparently slower temperature increase, in particular in case of the hollow sphere samples. Since all bulk and particulate samples have been prepared in a comparable way, this slow temperature increase cannot be assigned to the heating dynamics of the graphitic coating layers that may vary from sample to sample in a small and non-systematic way. When looking at longer measurement times, the relative magnitude of the first steplike process to the slower broad temperature increase is vastly different between the bulk and the particulate samples. Whereas for bulk

samples, only a small temperature increase can be assigned to the early radiative transport; it becomes the dominant transport mechanism for solid and hollow spheres. However, owing to the slow dynamics and high intensity, the established models are not capable of fitting these two processes anymore. The fitting model becomes increasingly inaccurate for temperatures above 525 °C (Figure S6, Supporting Information). Lunev et al. found a similar effect on alumina samples above 1000 °C and established a numerical model for their data.^[24]

For the hollow particles, the initial increase in temperature is reminiscent of the known temperature evolution of diffusive thermal transport. Even though radiative transport in non-scattering media is non-diffusive we, nevertheless, treated our measurement in a coarse approximation as a superposition of two diffusive transport processes based on the model of Cape and Lehman, which includes losses to the environment. Note that this simplified treatment uses the same diffusive thermal transport formalism for radiative and conductive transport. The temperature evolution was modeled as:

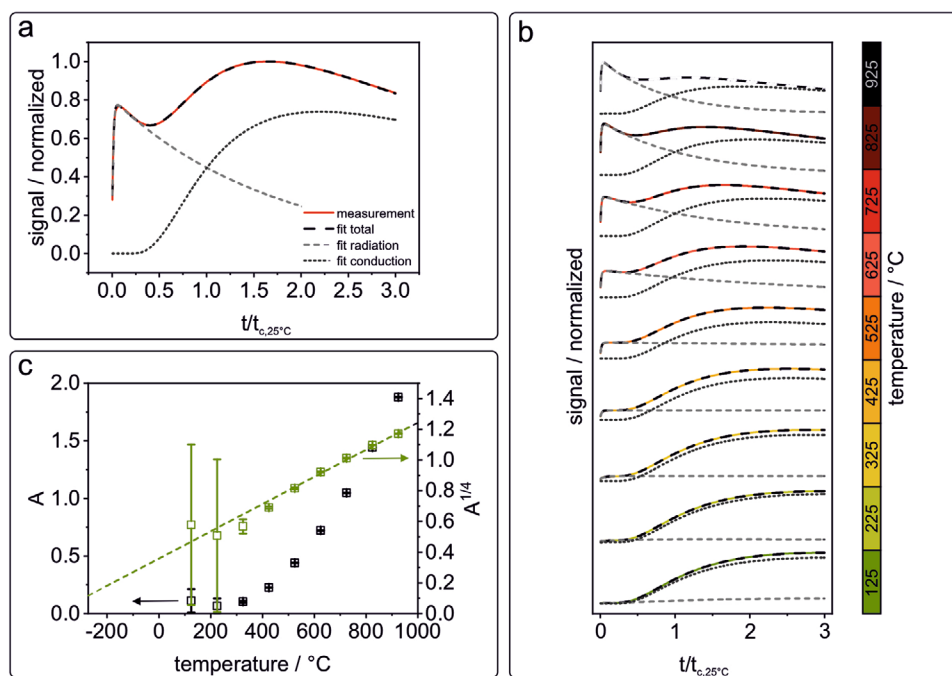


Figure 3. Double-diffusive model applied on 278 nm hollow particle measurements. a) Example of measurement at 725 °C. b) Application at all temperatures. c) Resulting ratio, A , of first and second diffusive process.

$$T(L, t) = A \sum_{m=0}^{\infty} C_{m,1} \xi_{m,1} e^{(\omega_{m,1}(t-\Delta)/t_{c,1})} + \sum_{m=0}^{\infty} C_{m,2} \xi_{m,2} e^{(\omega_{m,2}t/t_{c,2})} \quad (1)$$

A is a parameter for the ratio between the maximum intensities of the two processes, Δt is an initial time shift as the first process is not exclusively of diffusive nature.^[20]

$C_{m,i} = (-1)^m \frac{2\xi_{m,i}}{\xi_{m,i}^2 + 2H_i + H_i^2}$, where H_i represents the axial Biot number and $\xi_{m,i}$ is determined by $(\xi_{m,i}^2 - H_i^2)\tan(\xi_{m,i}^2) = 2\xi_{m,i}H_i$. Furthermore $\omega_{m,i} = -\frac{\xi_{m,i}^2}{\pi^2}$ and the characteristic time $t_{c,i} = \frac{L^2}{\pi^2\alpha}$.

An example of this data evaluation is shown in Figure 3a for the small hollow spheres at 725 °C (the evaluation of the big hollow particles can be found in Figure S7, Supporting information), where both transport processes display a similar order of magnitude. There is a convincing agreement between the measured data and the applied model, which can separate the individual transport processes. This simplified model is robust for a wide temperature range, where both processes occur (Figure 3b) and it could also be applied to the large hollow sphere sample (Figure S7, Supporting Information). Limitations of this model are conditions where one of the two processes strongly dominates, in the cases shown here at room temperature and > 900 °C. The intensity mismatch between the two processes is then too large and the fitting sensitivity insufficient for the weaker transport process. Another limitation is the timescale of the first diffusive process. The relatively slow temperature increase in case of the hollow sphere samples could be well-described. This was not possible for the solid particles anymore, where the radiative temperature increase was

slightly faster, as shown in Figure S5, Supporting Information. Nevertheless, we can extract from our simplified description, semiquantitative information (Figure S8, Supporting Information). The thermal diffusivity assigned to both processes should certainly only be taken as a rough estimate. The precondition of 1D heat transport is not valid anymore in this system, where two temperature gradients on different timescales are present within the sample. The thermal diffusivity of both processes differs by two orders of magnitude and shows a negligible temperature dependence in case of the slow, conduction-based process, whereas the fast process becomes significantly faster with increasing temperature. This is commensurate with previous reports on radiative thermal transport at high temperatures, where a strongly increasing thermal conductivity has been reported.^[25] Our model, furthermore, allows quantifying the temperature-dependent ratio, A , between the two processes, as shown in Figure 3c for the 278 nm hollow particle sample. This ratio follows a non-linear temperature dependency. It scales with T^4 , owing to its radiative nature obeying Stefan–Boltzmann’s law.^[11]

Having outlined the direct observation of such two transport processes, we now want to turn the focus on the influence of the optical properties onto the radiative transport. The transmission spectra are shown in Figure 4. We find that all samples are transparent in the IR detector region between 3 and 5 μm (yellow hatched area), except for the 8 μm solid silica particles. This correlates to the LFA results that did not show a distinct radiation peak for the 8 μm species. Optical transparency in this wavelength range is a precondition for radiative transport. Sub-micron sized TiO_2 hollow spheres, for instance, have a comparable mesostructure to the SiO_2 hollow spheres, yet, they are fully opaque from the UV/Vis to the MIR range (Figure S9,

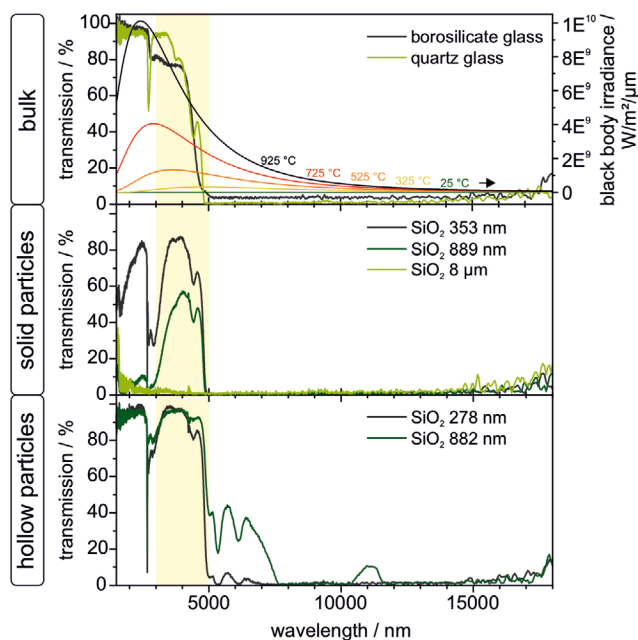


Figure 4. IR transmission data of bulk, solid particle, and hollow particle samples in comparison to black body irradiance. The LFA detection region between 3 and 5 μm is highlighted.

Supporting Information). Consequently, no radiative transport process could be observed (Figure S10, Supporting Information). A slight reduction of the mid-infrared transmission can be achieved by inert calcination conditions of the hollow spheres, which retain a small fraction of carbon in the particles. Whereas the optical appearance changed strongly (Figures S11 and S12, Supporting Information), the opacity in the 3–5 μm range was not sufficient to suppress the radiative process (Figure S13, Supporting Information).

To gain a deeper understanding of the radiative transport mechanism through such bulk and particulate materials, we used simulations based on the S-matrix method. These multi-body calculations have been performed on a simplified 2D multilayer model representing the most relevant structural parameters of our samples (Figure 5 left column). The model consists of top and bottom reservoirs representing the graphite coatings and in between, one bulk SiO_2 layer or several SiO_2 layers with a thickness of 353 and 20 nm gaps, representing the small solid particle structures. Here, the assumption was made that the interparticle distance is 6% of the particle diameter, which was calculated with a 3D radial distribution function of an MD simulated particle structure (Figure S14, Supporting Information). The big hollow particle structure is represented by 30 nm SiO_2 layers with 800 nm gaps, representing the hollow particle part, and 50 nm gaps, representing the interparticle distance. The calculated transmission spectra of the multilayer structure are in good agreement with the experimental data (Figure 5 middle column), and therefore, can be considered a reasonable approximation to the particle structure. These models allow calculating the transmission coefficients \mathcal{T}_j^{12} ($j = s, p$), which mainly determine the modes contributing to the radiative heat flow between the two graphite layers. They contain the contributions of waves that are propagating ($\kappa < k_0$)

and waves that are evanescent ($\kappa > k_0$) in vacuum, where κ is the wave vector component parallel to the interface and k_0 is the wavenumber in vacuum.^[26] Figure 5 (right column) shows the transmission \mathcal{T}_p^{12} , in the λ – κ plane. In case of bulk SiO_2 , radiative transport only occurs for wavelengths $< 5 \mu\text{m}$ with a considerable contribution of evanescent waves. In the transparency window, the lateral wave vector κ , which can propagate within SiO_2 , is limited by $\sqrt{\text{Re}(\epsilon_{\text{SiO}_2})}k_0 \approx 1.4 k_0$. In case of the solid sphere analogous structure, we find a layer dependence of the transmission coefficient. When increasing the number of layers from $N = 9$ to $N = 3121$ (Figure S15, Supporting Information), only waves in the transparency window with $\lambda < 5 \mu\text{m}$ can reach the second graphite layer. All other wavelengths are attenuated by the optical density of the SiO_2 particles. The solid spheres still show contributions of evanescent waves coupling to the graphitic reservoirs. It is interesting to note that there is no significant surface wave contribution in the reststrahlen band $\lambda = 8$ – $9.3 \mu\text{m}$. We elaborated on the role of surface modes within the reststrahlen band more explicitly using a numerically exact boundary element method provided by SCUFF-EM for 800 nm spheres (Figure S17, Supporting Information). This method takes far- and near-field contributions to the transmission function into account. For two adjacent SiO_2 particles, the heat flux is indeed dominated by a surface mode at $\lambda = 9 \mu\text{m}$. This mode, however, quickly attenuates when including more particles. Furthermore, when considering the transmission between two graphitic objects, the major contribution originates from modes with $\lambda < 8 \mu\text{m}$. This is due to the fact that damping of the coupled surface modes is too strong to ensure an efficient coupling over long distances. Considering the radiative transport case through hollow silica spheres, one recognizes the absence of evanescent contributions in \mathcal{T}_p^{12} . We attribute this to the increased distance between the silica surfaces. The major distance is governed by the hollow space (800 nm) inside of the silica capsules. The absence of evanescent waves is counteracted by a reduced optical density between $5 \mu\text{m} < \lambda < 7.5 \mu\text{m}$, where some transmission is also possible.

We used the transmission coefficients to calculate the heat transfer coefficients (htc), describing the radiative heat flow h^{12} from the graphite bottom at temperature T_1 and the heat flow h^{23} from the middle layer 2 at temperature T_2 toward the graphite top 3 at temperature T_3 , where h^{12} is for small time scales, the dominant contribution (see Supporting Information for details). The integrated htc of the multilayer models is shown in Figure 6 (left). The heat flow through the bulk silica film is larger than for the multilayer structure due to the larger contribution of the evanescent waves in the bulk film. Both particle structures feature comparable htc, which we rationalize by a compensation of the contributions of evanescent waves in case of the solid spheres and higher wavelength modes in case of the hollow spheres. Combining our double diffusive transport evaluation with the radiative transport analysis, we can draw several conclusions. Surface wave modes do not play a major role in the high-temperature transport through particulate SiO_2 materials – the reststrahlen band is too far red-shifted. The optical density of the particle packing determines which wavelengths can be transported through such structures, with a first window opening below 7.5 μm and the major contribution originating from $< 5 \mu\text{m}$. Evanescent

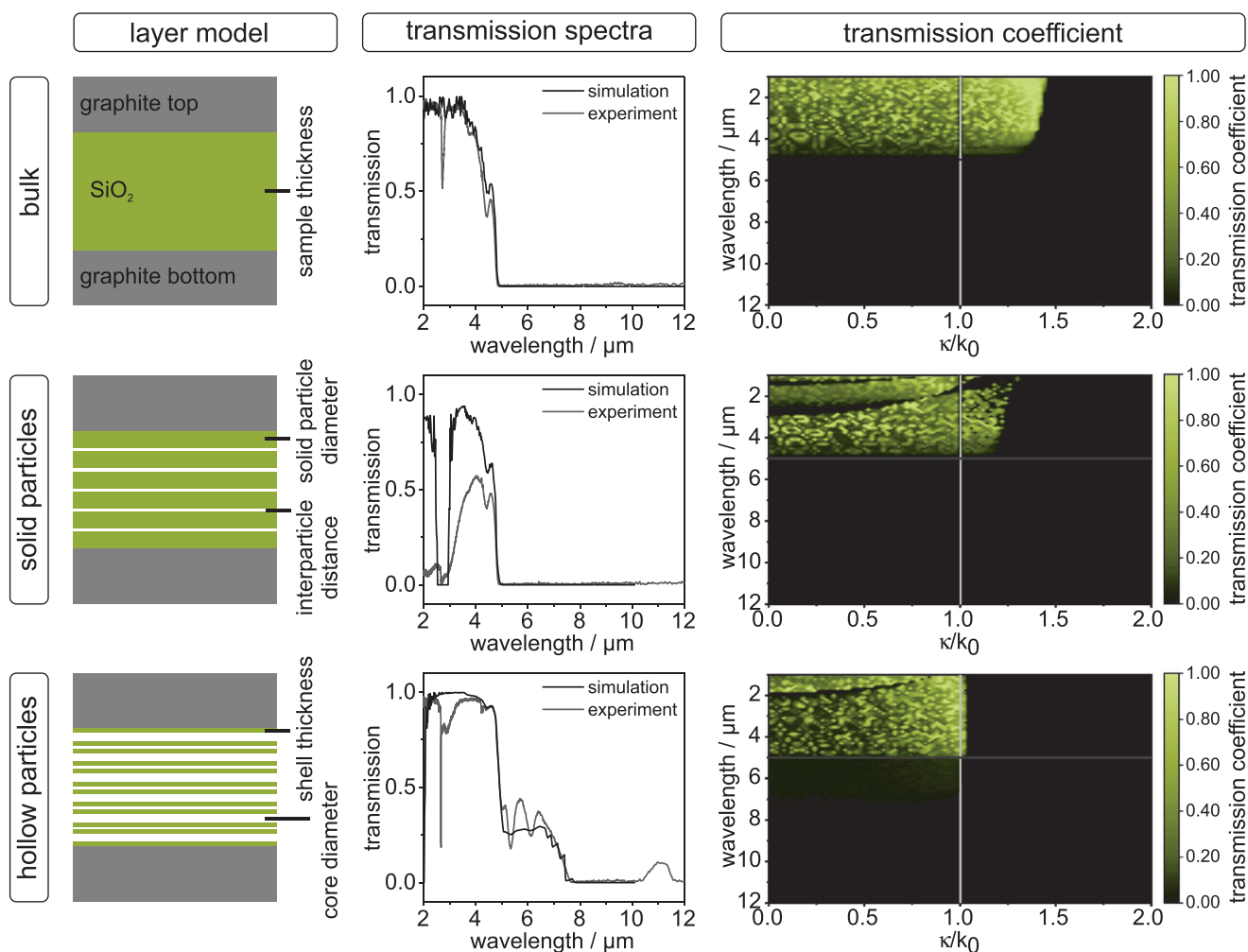


Figure 5. Left: Sketches of the layer model used for calculation of transmission spectra. Middle: Comparison between calculated and measured transmission spectra. Right: transmission coefficients of bulk, solid particle, and hollow particle structures.

waves are suppressed by the large porosity in the case of hollow silica beads.

We finally extended the multilayer model to also include thermal conduction through the individual layers (Figure 6,

right, see Supporting Information for details). This calculation is based on a set of coupled differential equations, which include the conductive and radiative heat flow between discrete layers. Two main conclusions can be drawn from this analysis.

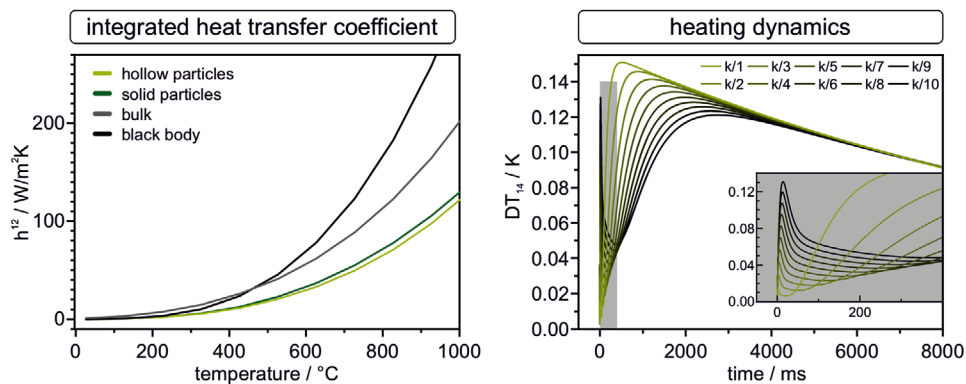


Figure 6. Integrated heat transfer coefficient h^{12} for hollow and solid SiO₂ particles, and bulk quartz glass, in comparison with black body radiation. The data was calculated using the multilayer model described in Figure 5 (left). Heating dynamics without lateral losses of the multilayer model from Figure S18, Supporting Information, at a temperature of 925 °C (right).

First, the main features of the time-dependent temperature evolution observed in the LFA experiment are well-captured by this analytic description. This corroborates our interpretation of the direct observation of a radiative and conductive heat transport process. Second, the systematic variation of the thermal conductivity of the solid skeleton stresses the importance of the relative heat transport capacity of these two channels. In case of a low conducting matrix, radiative transport becomes the dominant process. In case of a highly conducting matrix, radiative transport plays a subordinate role.

3. Summary and Conclusion

We demonstrated a direct observation of two distinct heat transport processes in mesostructured silica materials. We fabricated colloidal glasses comprising solid and hollow silica particles of 800 and 400 nm, respectively. The temperature evolution of the sample's top surface in an LFA experiment is dominated by a fast and a slow process. At room temperature, heat conduction along the silica network dominates, rendering such silica particle packings efficient thermal insulators comparable to polymer foams. With increasing temperatures, however, thermal radiation becomes more important and finally dominant, owing to the T^4 increase in radiation power and the blue shift of the radiated wavelengths. Optical transparency in the mid-infrared range and good thermal emitters at the boundaries are preconditions to open this radiative heat transport pathway. Consequently, these silica materials lose their room-temperature insulating behavior with increasing temperature. Surface wave modes within the reststrahlen band do not contribute to this radiative transport process. Evanescent waves, on the contrary, do contribute to the overall heat transport and are most prominent for bulk materials and ensembles of solid silica particles. The large intra-particle gaps caused by the hollow core in the case of silica capsules attenuates the contribution from evanescent waves. The radiative heat transport in hollow particle structures is slow enough to be described by a diffusive transport fit. Our results give a direct and detailed insight into the various transport mechanisms that govern high-temperature heat transport. Controlling the optical properties in the mid-infrared range either by means of the composition, the structure, or by adding additives is of paramount importance to maintain a strong thermal insulation behavior. The time-dependence of LFA measurements is a unique benefit to directly observe radiative and conductive thermal processes.

4. Experimental Section

Materials: Borosilicate glass (microscope slide, Menzel glass, Thermo Scientific) and quartz glass were cleaned with Hellmanex III (Hellma GmbH) and cut in pieces of 1×1 cm before the measurements. Sapphire discs ($d = 1$ cm, Edmund optics) were used as received.

SiO₂ solid particles in three different sizes (353 nm, 889 nm, and 8 μ m) were purchased from microParticles GmbH and used as received. The synthesis of the SiO₂ and TiO₂ hollow particles is described in detail in the Supporting Information.

The particles were assembled using the vacuum filtration method described by Ruckdeschel et al.^[27] A vacuum filtration system from Merck Millipore was used in combination with MF Millipore membrane filters

with pore sizes of 0.2 and 0.45 μ m. A Teflon funnel with a diameter of 1 cm was used for the SiO₂ particles. A funnel with a diameter of 1.2 cm was used for the TiO₂ particles because shrinkage of the samples during calcination had been considered. All samples had been dried at 40 °C in a vacuum overnight before calcination. The samples had been calcinated at 500 °C or 925 °C to remove organic components and avoid structural changes during the measurements.

Methods: UV-vis measurements were conducted on a Cary 5000 (Agilent Technologies) in transmission mode with the Ulbricht sphere in the range of 250 and 2500 nm. A holder for the round-shaped samples was 3D printed for UV-vis and IR measurements.

Infrared (IR) measurements were conducted on a VERTEX 70 spectrometer (Bruker) in the range of 1.5 and 18 μ m. Transmission measurements had been made using a gold-coated integrating sphere with an MCT detector.

Laser scanning microscopy was performed using a LEXT OLS5000-SAF microscope (Olympus) to determine the sample thicknesses and volumes.

Laser Flash Analysis was conducted on a LFA 467 HT HyperFlash apparatus (Netzsch) in the range of 25 °C and 925 °C under a slight nitrogen stream (50 mL min⁻¹). The samples were coated with a thin layer of graphite on the top and bottom side and placed in the sample holder, equipped with self-made graphite support and spacer (Figure 2c).

Supporting Information

Supporting Information is available from the Wiley Online Library or from the author.

Acknowledgements

The authors thank Stefan Rettinger and Tanja Feller for the help with STA and LEXT measurements, Thomas Tran for the determination of the mean particle distance and help with data evaluation, and Kishin Matsumori for some additional optical calculations. The authors also thank the Bavarian Polymer Institute, especially Ulrich Mansfeld and Markus Drechsler, for their help with SEM and TEM measurements. This project was funded by the German Research Foundation (DFG RE3550/2-1). T.L. acknowledges funding by ERC Starting Grant VISIRday under Grant No. 714968, and K.H. acknowledges funding by SFB840, TP B7. S.-A.B. acknowledges support from the Heisenberg Programme of the German Research Foundation (DFG, project No. 404073166).

Open access funding enabled and organized by Projekt DEAL.

Conflict of Interest

The authors declare no conflict of interest.

Data Availability Statement

The data that supports the findings of this study are available in the Supporting Information of this article.

Keywords

ceramic insulation, colloidal glasses, laser flash analysis, silica aerogels, thermal radiation

Received: August 21, 2021

Revised: October 7, 2021

Published online: November 9, 2021

- [1] A. Du, B. Zhou, Z. Zhang, J. Shen, *Materials* **2013**, 6, 941.
- [2] P. Ruckdeschel, A. Philipp, M. Retsch, *Adv. Funct. Mater.* **2017**, 27, 1702256.
- [3] a) E. Cohen, L. Glicksman, *J. Heat Transfer* **2014**, 136, 041301; b) J. Fricke, T. Tillotson, *Thin Solid Films* **1997**, 297, 212; c) U. Gross, L.-T.-S. Tran, *Int. J. Heat Mass Transfer* **2004**, 47, 3279; d) U. Heinemann, R. Caps, J. Fricke, *Int. J. Heat Mass Transfer* **1996**, 39, 2115; e) X. Lu, R. Caps, J. Fricke, C. T. Alviso, R. W. Pekala, *J. Non-Cryst. Solids* **1995**, 188, 226; f) G. Wei, Y. Liu, X. Zhang, F. Yu, X. Du, *Int. J. Heat Mass Transfer* **2011**, 54, 2355.
- [4] P. Ruckdeschel, M. Retsch, *Adv. Mater. Interfaces* **2017**, 4, 1700963.
- [5] S. A. Mofid, B. P. Jelle, X. Zhao, T. Gao, M. Grandcolas, B. Cunningham, S. Ng, R. Yang, *J. Build. Eng.* **2020**, 31, 101336.
- [6] M. Wiener, G. Reichenauer, S. Braxmeier, F. Hemberger, H. P. Ebert, *Int. J. Thermophys.* **2009**, 30, 1372.
- [7] J. Feng, J. Feng, Y. Jiang, C. Zhang, *Mater. Lett.* **2011**, 65, 3454.
- [8] P. Ruckdeschel, T. W. Kemnitzer, F. A. Nutz, J. Senker, M. Retsch, *Nanoscale* **2015**, 7, 10059.
- [9] S. N. Schiffres, K. H. Kim, L. Hu, A. J. H. McGaughey, M. F. Islam, J. A. Malen, *Adv. Funct. Mater.* **2012**, 22, 5251.
- [10] G. Wedler, H. J. Freund, *Lehrbuch der Physikalischen Chemie*, Wiley-VCH, Weinheim, Germany **2012**.
- [11] F. P. Incropera, D. P. DeWitt, T. L. Bergman, A. S. Lavine, *Fundamentals of Heat and Mass Transfer*, Wiley & Sons Ltd, Hoboken, NJ **2006**.
- [12] T. Xie, Y.-L. He, Z.-J. Hu, *Int. J. Heat Mass Transfer* **2013**, 58, 540.
- [13] a) S. Q. Zeng, A. Hunt, R. Greif, *J. Non-Cryst. Solids* **1995**, 186, 271; b) H. Liu, T. Li, Y. Shi, X. Zhao, *J. Mater. Eng. Perform.* **2015**, 24, 4054.
- [14] V. G. Parale, H.-N.-R. Jung, W. Han, K.-Y. Lee, D. B. Mahadik, H. H. Cho, H.-H. Park, *J. Alloys Compd.* **2017**, 727, 871.
- [15] S. A. Biehs, R. Messina, P. S. Venkataram, A. W. Rodriguez, J. C. Cuevas, P. Ben-Abdallah, *Rev. Mod. Phys.* **2021**, 93, 025009.
- [16] P. Ben-Abdallah, S.-A. Biehs, K. Joulain, *Phys. Rev. Lett.* **2011**, 107, 114301.
- [17] a) P. Ben-Abdallah, R. Messina, S.-A. Biehs, M. Tschikin, K. Joulain, C. Henkel, *Phys. Rev. Lett.* **2013**, 111, 174301; b) E. Tervo, M. Francoeur, B. Cola, Z. Zhang, *Phys. Rev. B* **2019**, 100, 205422.
- [18] D. Becerril, C. Noguez, *Phys. Rev. B* **2019**, 99, 045418.
- [19] N. Sakatani, K. Ogawa, Y. Iijima, M. Arakawa, R. Honda, S. Tanaka, *AIP Adv.* **2017**, 7, 015310.
- [20] J. A. Cape, G. W. Lehman, *J. Appl. Phys.* **1963**, 34, 1909.
- [21] A. Philipp, J. F. Eichinger, R. C. Aydin, A. Georgiadis, C. J. Cyron, M. Retsch, *Heat Mass Transfer* **2020**, 56, 811.
- [22] O. A. Sergeev, A. G. Shashkov, A. S. Umanskii, *J. Eng. Phys.* **1982**, 43, 1375.
- [23] L. F. Johnson, D. P. H. Hasselman, E. Minford, *J. Mater. Sci.* **1987**, 22, 3111.
- [24] A. Lunev, V. Zborovskii, T. Aliev, *Int. J. Therm. Sci.* **2021**, 160, 106695.
- [25] T. J. Shankland, U. Nitsan, A. G. Duba, *J. Geophys. Res: Solid Earth* **1979**, 84, 1603.
- [26] R. Messina, P. Ben-Abdallah, B. Guizal, M. Antezza, S.-A. Biehs, *Phys. Rev. B* **2016**, 94, 104301.
- [27] P. Ruckdeschel, A. Philipp, B. A. F. Kopera, F. Bitterlich, M. Dulle, N. W. Pech-May, M. Retsch, *Phys. Rev. E: Stat., Nonlinear, Biol., Soft Matter Phys.* **2018**, 97, 022612.